

Hydrodynamics and dilution of an oil jet in crossflow: The role of small-scale motions from laboratory experiment and large eddy simulations



Cosan Daskiran^a, Fangda Cui^a, Michel C. Boufadel^{a,*}, Lin Zhao^{b,1}, Scott A. Socolofsky^c, Tamay Ozgokmen^d, Brian Robinson^e, Thomas King^e

^a Center for Natural Resources, Civil and Environmental Engineering Department, New Jersey Institute of Technology, Newark, NJ 07102, United States

^b ExxonMobil Upstream Research Company, Houston, TX 77389, United States

^c Zachry Department of Civil Engineering, Texas A&M University, College Station, TX 77843, United States

^d Department of Ocean Sciences, University of Miami, Miami, FL 33149, United States

^e Bedford Institute of Oceanography, Department of Fisheries and Oceans, Dartmouth, Canada

ARTICLE INFO

Keywords:

Jet in crossflow
Large eddy simulation
Oil jet
Counter rotating vortex pair
Wake vortices

ABSTRACT

Experimental results were presented for the release of diesel oil from a one-inch (2.5 cm) vertical pipe in a crossflow at 0.27 m/s. The ratio of jet velocity to crossflow speed was 5.0 and the Reynolds number based on jet velocity and pipe diameter was 7.1×10^3 . In the experiments, the plume shape was photographed, and the oil droplets were measured at two vertical locations on the center axis of the plume. Acoustic Doppler velocimetry (ADV) data was also obtained and compared to numerical predictions. The plume was simulated using large eddy simulation (LES), and the mixture multiphase model. The impact of the oil buoyancy was captured by adding a transport term to the volume fraction equation. Using the rise velocity based on d_{50} (volume-median) droplet size in the lower part of the plume allowed us to capture the lower boundary of the plume, but the estimated upper boundary of the plume penetrated less into the crossflow as compared to the experimental findings. However, using the rise velocity of the d_{50} at the upper part of the plume allowed one to estimate the upper boundary of the plume. As the droplets are too small to be resolved by the LES, we could not use a systematic approach to allow the multiphase plume to spread to mimic the observations. Based on the simulation results, the interaction between the jet and crossflow yielded small-sized flow structures near the upper boundary of the plume. The wake vortices initiated from the leeward side of the plume showed an alternating vorticity pattern in the wake. The shear layer vortices were induced by Kelvin-Helmholtz instabilities mostly on the windward side of the plume. The formation of counter rotating vortex pair (CVP) altered greatly the hydrodynamics of the jet from that of a vertical jet to manifest flow reversals in all directions. The formation of CVP is likely to enhance the mixing of chemicals and droplets within the plume.

1. Introduction

The hydrodynamics of miscible jets (i.e. water in water) has been extensively studied since the work of Morton et al. (1956), and the applications are varied (Fischer et al., 1979), including outfalls of manufacturing plants, sewage plants discharges, release of exhaust plumes and fire plumes (McGrattan et al., 1998, Ma and Quintiere, 2003, Hunt and Van den Bremer, 2011). Immiscible jets of liquid in air have also received wide attention to the interest in combustion where liquid fuel is released into air chambers (Sallam and Faeth, 2003, Shinjo et al., 2009, Som and Aggarwal, 2010, Shinjo and Umemura, 2011). Immiscible jets of gas in water (bubbles) have also received wide

attention due the interest of using air flow to mix fluids (Lima Neto et al., 2008) and the release of natural gas from underwater vents (MacDonald et al., 2002, Leifer et al., 2015). But there is much less work on the release of immiscible liquids in liquid. Salient works include that of Socolofsky and Adams (2002) who documented the separation of individual droplets and bubbles from multiphase plumes. The study of immiscible jets received renewed interest following the Deepwater Horizon (DWH) spill which released estimated amounts of 450,000 to 700,000 tons of oil (McNutt et al., 2011) and 500,000 tons of gaseous hydrocarbons into the Gulf of Mexico (Joye et al., 2011). Socolofsky et al. (2011) investigated the general transport of the DWH multiphase plume using dimensional arguments, and their results

* Corresponding author.

E-mail address: boufadel@gmail.com (M.C. Boufadel).

¹ Work was completed while the author was a Postdoc at New Jersey Institute of Technology.

matched closely observations in terms of the formation of an intrusion layer due to seawater stratification.

Simulation studies of plumes have also gained interest. [Fabregat et al. \(2015, 2016\)](#) used a hybrid approach of miscible fluid with a rise velocity for the bubbles to capture the behavior of the DWH plume. [Yang et al. \(2016\)](#) used Large Eddy Simulation (LES) to investigate the mechanisms of buoyancy and trap height in the DWH. The DWH plume was in a stratified environment due to the large release flow with respect to crossflow and due to ocean stratification. However, there are numerous situations where crossflow is dominant causing the bending of the plume, and the separation of oil droplets ([Socolofsky and Adams, 2002](#), [Murphy et al., 2016](#)) and gas bubbles ([Socolofsky et al., 2002](#)) from the plume. We present herein the results of an experimental study and a numerical investigation, with a focus on the latter. For this reason, we provide below a brief review on the simulation of jets/plumes in crossflows.

The hydrodynamics and vortical structures for a jet in crossflow were studied by several researchers ([Yuan et al., 1999](#), [Gopalan et al., 2004](#), [Muppudi and Mahesh, 2007](#), [Mahesh, 2013](#), [Behzad et al., 2016](#)). [Yuan et al. \(1999\)](#) revealed spanwise rollers on leading and trailing edges of the jet which are induced by Kelvin-Helmholtz (K-H) instabilities and primarily responsible for the near-field turbulent kinetic energy (t.k.e.) production. PIV techniques were used by [Gopalan et al. \(2004\)](#) to investigate the flow structures at low jet-to-crossflow velocity ratios (r) varying from 0.5 to 2.5. At $r < 2$, the positive K-H vortices along the leading edge of the jet was suppressed due to the interaction with negative crossflow boundary layer vortices. A reverse flow was observed behind the jet inside a semi-cylindrical vortical layer. For $r > 2$, reverse flow was not observed, instead vortices similar to Karman vortex street was obtained. The jet in crossflow promotes mixing as compared against the jet into stationary fluid. For jet in crossflow, the interactions between the jet fluid and the crossflow yields different types of coherent vortical structures ([Fric and Roshko, 1994](#)) such as counter rotating vortex pair (CVP) and wake vortices. [Muppudi and Mahesh \(2007\)](#) performed single phase direct numerical simulation (DNS) of a jet in crossflow. They computed t.k.e. budgets through the fluctuating velocity component and its derivatives. In the near field, the t.k.e. production made peak along the leading edge of the jet while the peak t.k.e. dissipation was obtained along the trailing edge of the jet. However, due to the formation of CVP vortices in the far field, the maximum production was near the leeward side of the plume and the maximum dissipation was located toward the upper surface of the plume.

Several studies investigated the turbulent mixing for a jet in crossflow ([Muldoon and Acharya, 2006](#), [Bodart et al., 2013](#), [Coletti et al., 2013](#), [Galeazzo et al., 2013](#), [Ling et al., 2017](#), [Ryan et al., 2017](#)). Most of them are focused on film cooling applications in gas turbines in which the coolant jet was injected into a crossflow. [Muldoon and Acharya \(2006\)](#) computed all the exact terms in $k - \epsilon$ model through direct numerical simulations (DNS) and compared against the modelled terms in standard $k - \epsilon$ turbulence model. Although, they observed reasonable agreement for many of the terms, the eddy diffusivity modelled in standard $k - \epsilon$ turbulence model provided significant discrepancy. [Bodart et al. \(2013\)](#) conducted large eddy simulations of an inclined jet in crossflow for film cooling systems. They reported that the misalignment between the scalar flux term and the concentration gradient term was reasonable on vertical and spanwise directions, however

they observed large misalignment in streamwise direction which was related to the large coherent structures in the jet. [Galeazzo et al. \(2013\)](#) compared measured Reynolds stress and scalar flux components against the numerical simulation results predicted through LES and Reynolds-averaged Navier-Stokes (RANS) modeling. The LES results of mean variables and fluctuating components agreed well with the measurements. However, the predicted turbulent Schmidt number, Sc_t in crossflow direction along the center plane did not agree well with the Sc_t from the measurements. They argued that the equations used to compute the Sc_t was derived assuming the turbulence only source of fluctuation which is not the case in regions where the coherent structures developed.

In this work, multiphase liquid jet in liquid crossflow including surface tension forces among the phases were considered. High-fidelity large eddy simulation coupled with mixture model was conducted. The trajectory of the plume and the dilution of oil along the jet path were compared against our experiments and integral solution by [Jirka \(2004\)](#), respectively. Initially, the standard solver was used, however the comparison of predicted plume trajectory to the one observed in our experiments revealed that the predicted plume penetrated less into the crossflow. The solver was modified to include an additional advection term due to the rise velocity of droplets and a good agreement was obtained. The hydrodynamics and mixing induced by different vortical structures for an oil jet in crossflow were presented and discussed.

2. Methods and materials

2.1. Experimental setup

The experimental facility is the Ohmsett tank ([www.ohmsett.com](#)) in Leonardo, New Jersey. The tank is 203 m in length, 20 m in width and 2.4 m in depth. The oil jet was released vertically and the whole system was towed in the tank at the speed of 0.27 m/s, which mimicked the crossflow. The towing started prior to the release of the oil. The inside diameter of the pipe was 2.5 cm (1-inch) with a vertical length of 50 cm. Fuel Oil #2 was used as the jet fluid, and the properties of the oil are reported in [Table 1](#). The oil flow rate was 40 L/min and the velocity inside the pipe was 1.36 m/s, this resulted in jet-to-crossflow velocity ratio ($r = u_{oil}/u_\infty$) of 5.0. The velocity ratio has been used by several researchers to characterize the hydrodynamics of a jet in crossflow ([Friedman and Katz, 2002](#), [Muppudi and Mahesh, 2007](#), [Milanovic et al., 2012](#), [Mahesh, 2013](#)).

The time series of velocity at different positions was measured using Acoustic Doppler Velocimetry (ADV). The photograph of the metallic frame with all instruments installed is shown in [Fig. 1](#). Four ADVs (Nortek AS) numbered in [Fig. 1](#) were used to measure the time series of velocity in three-dimensions. The frequency of ADV1 and ADV2 (Vectrino Vector, Nortek Inc.) which are designed for field experiments was 8 Hz. The frequency of ADV3 (Vectrino Profiler, Nortek Inc.) and ADV4 (Vectrino Probe, Nortek Inc.) was 100 Hz and 200 Hz, respectively. The signal to noise ratio (SNR) and correlation coefficient are two major parameters to evaluate the accuracy of ADV data. The SNR varies based on particle seeding concentration. The correlation coefficient is related to the uncertainty in the velocity. The correlation coefficient of 60% or higher was suggested by [McLellan and Nicholas \(2000\)](#). The SNR higher than 5.0 provides mean velocity components while the SNR higher than 15.0 is required for instant velocity measurement ([Nortek,](#)

Table 1

The parameters used in experiment and simulation.

Parameter-Value-Unit							
Q_{oil}	40	[liter/min]	u_{oil}	1.36	[m/s]	u_∞	0.27
ρ_{oil}	840	[kg/m ³]	μ_{oil}	4.0×10^{-3}	[kg/ms]	σ	0.0256
$\rho_{seawater}$	1025	[kg/m ³]	$\mu_{sea-water}$	1.1×10^{-3}	[kg/ms]	d_{in}	[m]

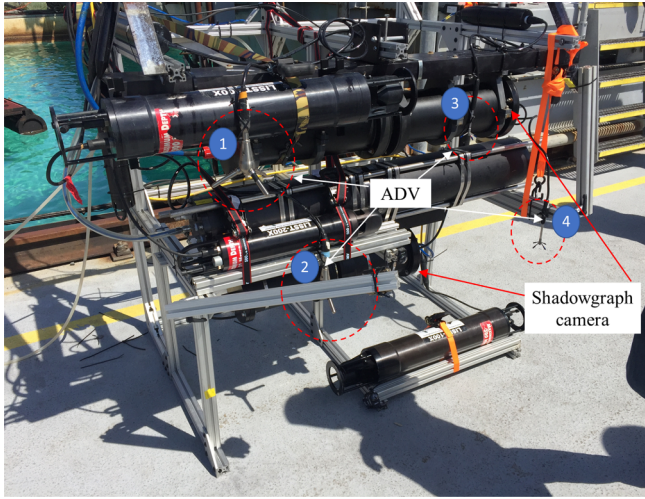


Fig. 1. Metallic frame used to hold all instruments including four ADVs and two shadowgraph cameras. The metallic frame was towed with the pipe. The horizontal distance between the pipe and the metallic frame was around 2 m.

Table 2
Position of the velocity measurement relative to the center of pipe exit.

	x [m]	y [m]	z [m]
ADV1	1.39	-0.48	1.24
ADV2	1.46	-0.25	0.81
ADV3	1.55	0.34	1.29
ADV4	1.47	0.65	0.88

1998, McLlland and Nicholas, 2000). In this work, the velocity data acquired from the ADVs with $\text{SNR} < 15$ and the correlation coefficient lower than 60% were excluded. The position of the velocity measurement is provided in **Table 2** relative to the origin placed at the center of the pipe exit. The oil droplet size distribution was measured using two shadowgraph cameras to reveal the droplet size near the upper and lower boundaries of the plume (**Fig. 1**).

The Reynolds numbers (Re) at the pipe entrance and the crossflow inlet are defined as follows:

$$Re_{oil} = \frac{\rho_{oil} u_{oil} d}{\mu_{oil}} \quad (1a)$$

$$Re_{\infty} = \frac{\rho_{seawater} u_{\infty} d}{\mu_{seawater}} \quad (1b)$$

Here, ρ is density, μ is dynamic viscosity, u_{oil} is the velocity at pipe entrance with top hat profile, u_{∞} is the upstream velocity (or crossflow speed) and d is the pipe diameter.

Jet in crossflow hydrodynamics of miscible fluids has been addressed in various works (Cheung, 1991, Tian and Roberts, 2003, Muppudi and Mahesh, 2007), and Jirka (2004) developed an integral model. As we will be comparing our numerical results to that model, some fundamental properties of the model are introduced herein. They are based on various works in the literature (Wright, 1977, Jirka and Domeker, 1991, Jirka, 2004):

The discharge length scale L_Q is given by:

$$L_Q = \frac{Q_o}{\sqrt{M_o}} \quad (2a)$$

where $Q_o = u_o a_o$ and $M_o = u_o^2 a_o$

Here, Q_o is the volumetric flux and M_o is the momentum flux. The term u_o is the velocity at the orifice and a_o is the cross-sectional area of the pipe.

The jet-to-crossflow transition length scale L_m defines the region

where the flow regime changes from weakly deflected to strongly deflected and it is given by:

$$L_m = \frac{\sqrt{M_o}}{u_{\infty}} \quad (2b)$$

The plume-to-crossflow transition length scale L_b defines the length of the plume penetration beyond which the plume is deflected highly by the crossflow and it is given by:

$$L_b = \frac{J_o}{u_{\infty}^3} \text{ where } J_o = u_o a_o g' \quad (2c)$$

Here, J_o is the buoyancy flux at orifice and g' is the reduced gravity given by $g' = \frac{(\rho_c - \rho_d)}{\rho_c} g$ where ρ_c and ρ_d is the density of continuous and dispersed phase, respectively, and g is the acceleration of gravity.

The jet-to-plume transition length scale L_M differentiate the region dominated by initial momentum of the flow (jet-like) from buoyancy dominant region (plume-like) and it is given by:

$$L_M = \frac{M_o^{3/4}}{\sqrt{J_o}} \quad (2d)$$

And the centerline dilution is given by:

$$S_c = \frac{c_o}{c_c} \quad (2e)$$

Here, c_o is the centerline concentration at the orifice and c_c is the centerline concentration along the plume. Of interest is the normalized centerline dilution, $S_c L_Q L_m / L_b^2$ as a function of normalized vertical distance, z/L_b .

2.2. Simulation setup

The upstream and side views of the computational domain with geometric details are shown in **Fig. 2**. The crossflow is in the x -direction, and the jet is in the z -direction. The origin was placed at the center of the pipe orifice (jet exit). The pipe entrance was placed 0.2 m above the channel bottom to make it closer to our experiments in which the pipe was towed. The horizontal distance between the crossflow inlet and the pipe was set to be 4.0 m while the outlet was placed 6.0 m away from the pipe. The distance between the orifice and the water free surface was 1.7 m.

At the pipe inlet, a top-hat velocity profile was defined in the vertical direction. The uniform water velocity of 0.27 m/s in the horizontal direction was assigned as upstream boundary condition for the domain. No velocity perturbations were imposed on either the upstream side of the domain nor on the oil flow inlet (**Fig. 2b**). In the experiments, as the pipe was towed into a quiescent water body, the leading edge of the jet and the upper boundary of the plume was exposed to nearly no-perturbed flow which was mimicked in the simulation by assuming no-perturbation at the crossflow inlet. The Reynolds number (Re) at the pipe entrance and the crossflow inlet were computed to be 7.1×10^3 and 6.5×10^3 , respectively (Eq. (1)). The parameters used in the simulation set up and their values are listed in **Table 1**. At the outlet, zero-gradient condition was assigned for the velocity and gauge pressure of 0 Pa was assigned for the pressure. No-slip condition was adopted inside and outside the pipe surfaces and the bottom surface of the computational domain. Zero-shear (*free-slip*), no penetration boundary condition was applied for the side boundaries of the domain to prevent the effects of boundary layer in the flow. The top boundary was also set to zero-shear condition, as there was no major wind blowing on the water surface during the experiment, and thus the stress is expected to be minimal.

Initially, a top hat velocity profile was assigned in the pipe. Outside of the pipe, the crossflow velocity of 0.27 m/s was set in crossflow-wise direction. The oil holdup was set to be unity inside the pipe and zero outside the pipe. The time-averaging was started after the flow evolved for 10.35 s, which stands for 112 characteristics time units, d/u_{∞} . The

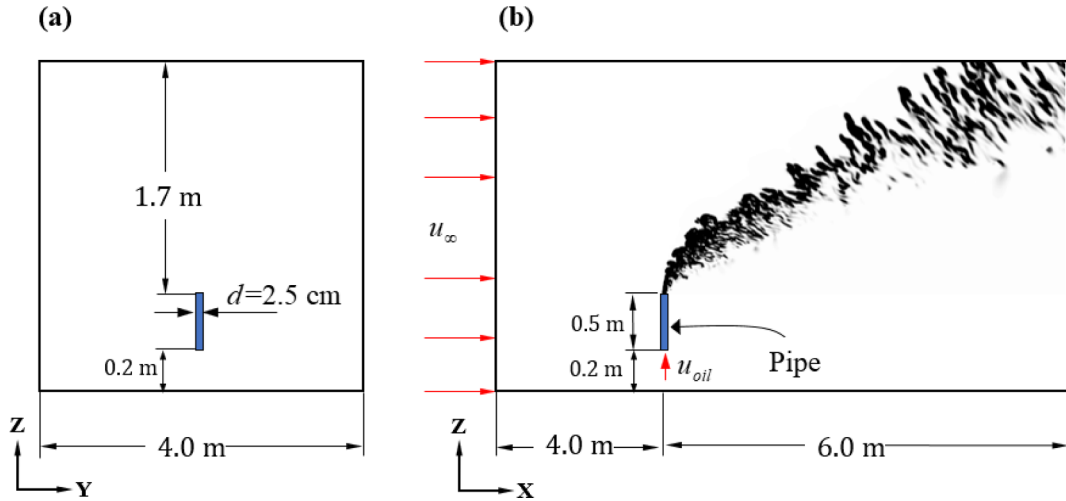


Fig. 2. Front and side view of the computational domain with geometric details for oil jet in crossflow. The pipe diameter is one-inch (2.5 cm) and the pipe length was 50 cm.

mean flow variables presented in this paper were then computed over another 100-time units between 10.35 s and 19.5 s.

The contours of cell size along the center plane and at different cross-sections (y - z plane) are shown in Fig. 3. The mesh was refined for the region where oil plume was expected based on the experimental results (Fig. 4). The mesh near the pipe surface, and the top and bottom surfaces of the computational domain were also refined. The mean cell size (called filter size, Δ) was computed as $\Delta = V^{1/3}$ where V is the cell volume. The mean cell size in the plume region was in the range of

2 mm to 8 mm (Fig. 3). The mesh spacing outside of the expected region of the oil plume was increased to 32 mm and then 64 mm near the domain boundaries. The mesh elements were mainly hexahedral, and the whole domain was discretized using 20 million cells. The computational domain was divided into subdomains to reduce the cell size away from the region of interest. Non-conformal mesh interfaces were used to couple the subdomains. The flow field variables were exchanged among the subdomains during the transient, iterative solution.

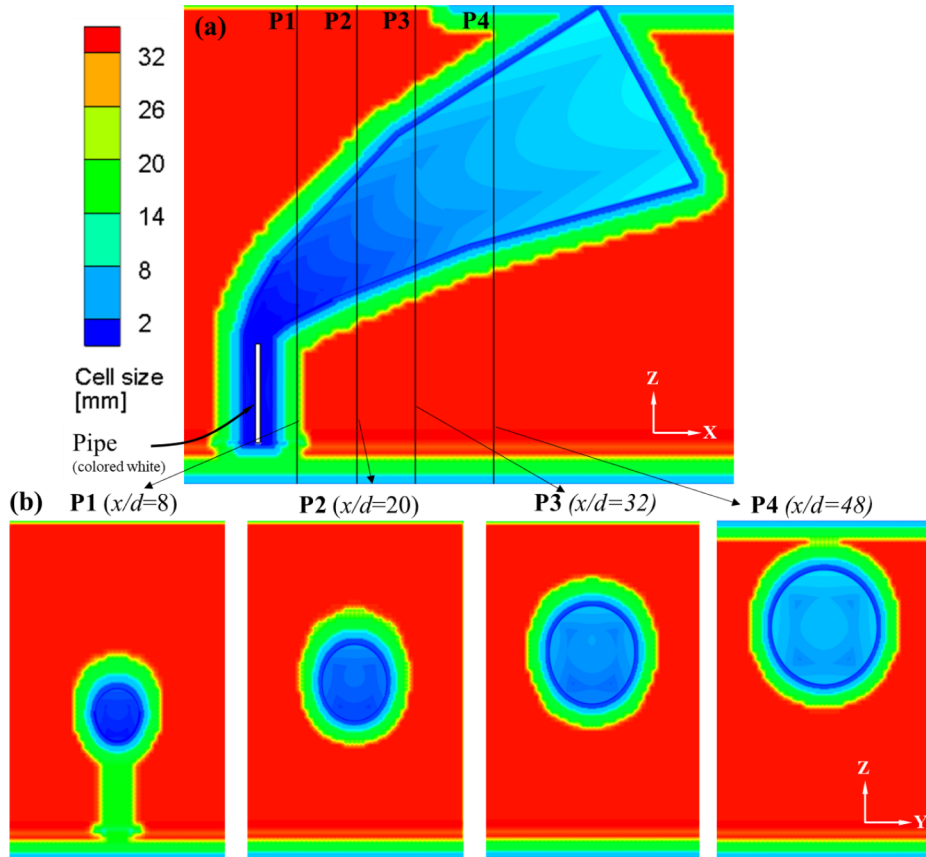


Fig. 3. Contours of cell size along (a) the center plane and (b) different cross-sections of the computational domain labeled as P1 ($x/d = 8$), P2 ($x/d = 20$), P3 ($x/d = 32$) and P4 ($x/d = 48$). The black lines on the center plane indicate the location of the cross-sections in (b).

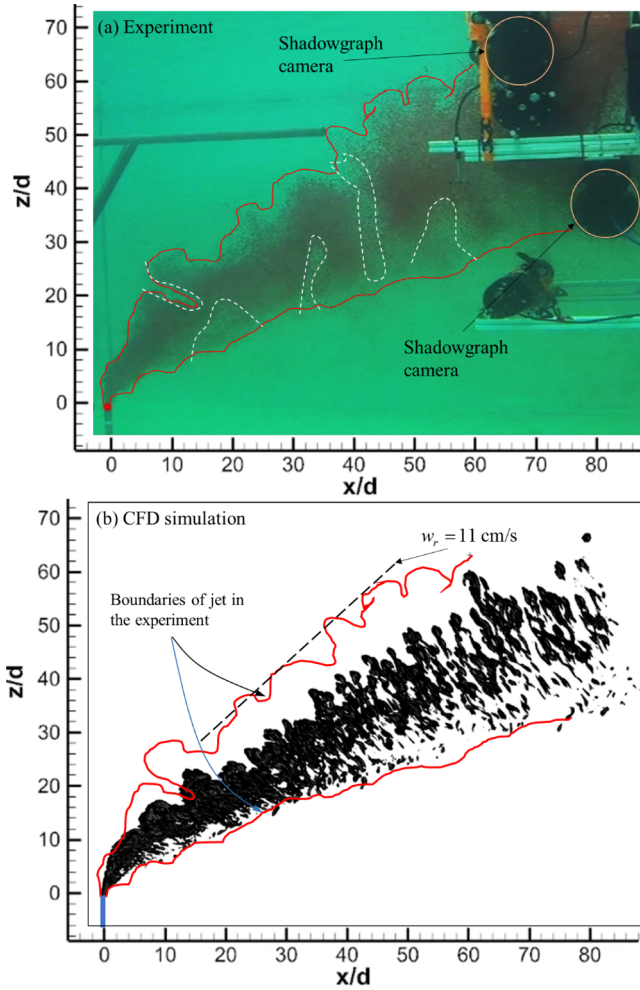


Fig. 4. (a) Snapshot of the oil plume during the experiment, the red line denotes the plume boundaries and re-plotted in (b). Note the clearance (small amount of oil) between the oil clouds shown by white dashed lines at $x/d = 14$, $x/d = 32$, $x/d = 42$ and $x/d = 54$, (b) instantaneous iso-surfaces of oil holdup at 0.05 predicted by the simulation with rise velocity of 5 cm/s. The dashed lines in (b) show estimated upper boundary of the plume based on the rise velocity of 11 cm/s (Friedman and Katz, 2002) using the droplet size measured by the upper shadowgraph camera. (For interpretation of the references to colour in this figure legend, the reader is referred to the web version of this article.)

3. Mathematical model and numerical approach

In this study, the open source software package of OpenFOAM was utilized. The modified solver was based on the mixture multiphase model (Manninen et al., 1996; Qu et al., 2011; Yousefi-Lafouraki et al., 2016) in which continuity and momentum equations are solved for the mixture. A transport equation for the volume fraction was also solved to predict the spatial and temporal distribution of the two phases (oil and water). The turbulent flow was modeled using a high-fidelity large eddy simulation (LES) turbulence model (Yuan et al., 1999; Bodart et al., 2013; Galeazzo et al., 2013; Ruiz et al., 2015; Ryan et al., 2017) in which the eddies larger than the filter size are resolved and the smaller ones are modelled through sub-grid scale (SGS) models. The filtered form of the incompressible Navier-Stokes equations is:

$$\nabla \cdot u = 0 \quad (3)$$

$$\frac{\partial u}{\partial t} + u \cdot \nabla u = -\frac{1}{\rho_m} \nabla p_{rgh} + v_m \nabla^2 u - \nabla \cdot \tau^r + F_{st} - \frac{\nabla \rho_m}{\rho_m} g e_3 \quad (4)$$

Here, u is the mixture velocity, p_{rgh} is the resolved pressure excluding hydrostatic pressure, ρ_m is the mixture density and v_m is the

kinematic viscosity of the mixture. For incompressible flow, the time derivative of density in the original form of Eq. (3) drops out. The terms on the left-hand side of Eq. (4) is called the inertial term including the time derivative of velocity which disappears in steady state solutions and the advection term, respectively. The first term on the right-hand side represents the acceleration due to pressure gradient, the second term is the acceleration due to viscous forces (shear stress) and the third term represents the sub-grid scale stress tensor which will be detailed later. The external force term, F_{st} represents the surface tension forces between the two phases. It was modeled herein using the continuum surface force (CSF) approach proposed by Brackbill et al. (1992), which converts the surface forces to volume forces using the Green theorem (Francois et al., 2007). The last term is the buoyancy term in the vertical direction where e_3 represents the unit vector in the vertical direction. The mixture density and dynamic viscosity was computed using the phase volume fraction as follows:

$$\rho_m = \mu_d \alpha_d + \rho_c \alpha_c \quad (5a)$$

$$\mu_m = \mu_d \alpha_d + \mu_c \alpha_c \quad (5b)$$

where α_d is the volume fraction of oil (thus a value of 1.0 implies 100% oil) and α_c is the volume fraction of water. The subscripts d and c represent the discrete (oil) and continuous (water) phases, respectively. Note that $\alpha_d + \alpha_c = 1.0$. Although the mixture density varies based on the volume fraction and densities of each fluid, the incompressible flow and Bousinesq approximation were adopted herein since the density variation is small. The oil and water densities are close to each other and oil is diluted quickly due to water entrainment which makes the mixture density close to the water (ambient fluid) density by $x/d = 20$. Moreover, the density of oil and water phases were taken to be constant. It must be noted here that the buoyancy forces induced by the density difference was considered by following the Bousinesq approximation.

The sub-grid scale stress tensor, $\tau_{ij}^r = \widetilde{u_i u_j} - \widetilde{u_i} \widetilde{u_j}$ occurred due to the filtering operation was computed through SGS modeling. The deviatoric part of SGS stress, $\tau_{ij}^r - \frac{1}{3} \tau_{kk}^r \delta_{ij}$, can be modeled based on the strain rate tensor, S_{ij} by following the Boussinesq hypothesis (Pope 2000):

$$\tau_{ij}^r - \frac{1}{3} \tau_{kk}^r \delta_{ij} = -2v_{SGS} S_{ij} \quad (6)$$

where τ_{kk}^r is the isotropic part of the SGS stress which can be neglected or added to the filtered pressure in incompressible flows (Erlebacher et al., 1992), δ_{ij} is the Kronecker delta, v_{SGS} is the SGS eddy viscosity, and $S_{ij} = \frac{1}{2} \left(\frac{\partial u_i}{\partial x_j} + \frac{\partial u_j}{\partial x_i} \right)$ is the strain-rate tensor. In this work, the Smagorinsky SGS model (Smagorinsky, 1963) was employed to predict SGS eddy viscosity, given by:

$$v_{SGS} = (C_S \Delta)^2 |S| \quad (7)$$

where $S = \sqrt{2S_{ij} S_{ij}}$ and C_S is the Smagorinsky constant, taken as 0.168 in the present study and Δ is the local grid size.

In the standard solver, an advection equation for the volume fraction is solved to track the interface between the phases. However, to account for the slip velocity between oil and water (due to the rise of oil droplets in water), and the diffusion of oil in water, the volume fraction equation was modified as follows (Fabregat et al., 2016; Yang et al., 2016):

$$\frac{\partial \alpha_d}{\partial t} + \nabla \cdot (\alpha_d u) + \nabla \cdot (\alpha_d (1 - \alpha_d) u_c) = (D_b + D_{SGS}) \nabla^2 (\alpha_d) - w_r \frac{\partial \alpha_d}{\partial z} \quad (8)$$

Here, u_c is the compression velocity, which is an artificial term introduced by Rusche (2003) to counteract the numerical diffusion at the interface. The compression velocity represents the maximum velocity in the transition region perpendicular to the interface. The first term on the right-hand side represents the diffusion of oil in water which is induced by the gradient of the discrete phase volume fraction. The

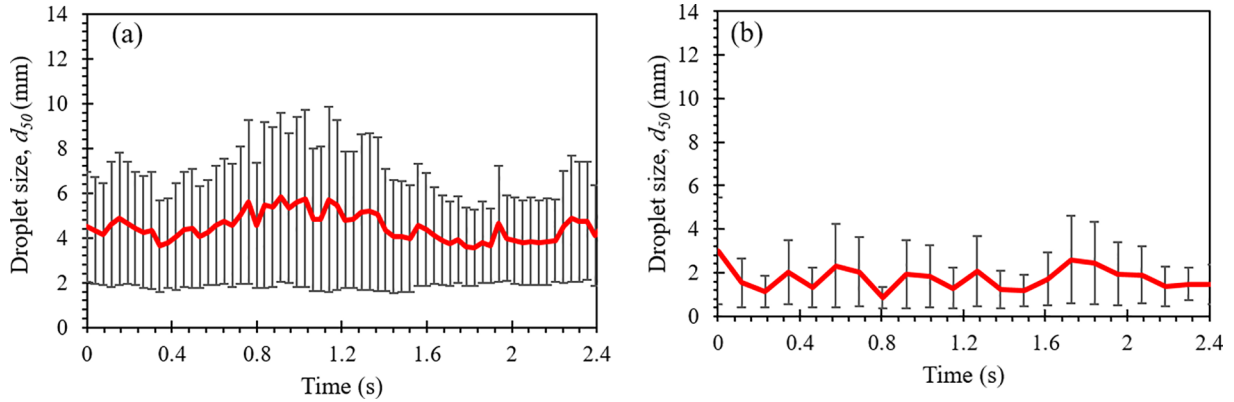


Fig. 5. Time series of median diameter, d_{50} from (a) top and (b) bottom shadowgraph cameras. The d_{50} varies over the time. The standard deviation is the deviation of d_{50} from the image at given time to prior image. The frequency of top camera is 24 fps while it is 8 fps for bottom camera. Time-averaged d_{50} from top and bottom cameras was 4.4 mm and 1.6 mm, respectively. Time-averaged d_{50} from bottom camera was used in the simulation as the rise velocity of droplets.

molecular diffusion coefficient of oil in water D_b at 20 °C was taken to be $1.12 \times 10^{-8} \text{ m}^2/\text{s}$ (Hamam, 1987). The sub-grid scale diffusion coefficient D_{SGS} was computed based on sub-grid Schmidt number ($Sc_{SGS} = 0.7$) and sub-grid eddy viscosity v_{SGS} in Eq. (7). The last term on the right-hand side represents the convection term induced by the oil rise velocity in vertical direction, w_r . The terminal rise velocity of droplets was computed based on the experimental measurements by Friedman and Katz (2002). Once the α_d is computed by Eq. (8), the volume fraction of the water (α_c) can be determined as $(1 - \alpha_d)$ as mentioned earlier.

The Navier-Stokes equations (Eqs. (3) and (4)) were solved through the combination of two algorithms: Pressure Implicit with Splitting of Operators (PISO) and Semi-Implicit Method for Pressure-Linked Equations (SIMPLE). The divergence and laplacian terms in Eqs. (3), (4) and (8) were discretized using second order discretization schemes. The first order, Euler discretization scheme was used for time since it was stable. The adjustable time step size was selected based on the Courant–Friedrichs–Lowy condition (CFL) number less than unity which yielded time step size of nearly $7 \times 10^{-5} \text{ s}$ after the flow reached quasi-steady behavior.

The resolved turbulent kinetic energy is computed as follows:

$$k_{res} = \frac{1}{2}(\bar{u}'_i)^2 \quad (9)$$

$$u'_i = u_i - \bar{u}_i \quad (10)$$

Here, u'_i is the turbulent component of velocity, u_i is the resolved velocity by LES and \bar{u}_i is the time-averaged velocity. A measure of turbulence resolution can be evaluated by the ratio of resolved turbulent kinetic energy to total turbulent kinetic energy as follows (Pope, 2004, Wegner et al., 2004):

$$M = \frac{k_{res}}{k_{res} + k_{SGS}} \quad (11)$$

The value of M varies between 0 and 1. $M = 0$ corresponds to RANS while $M = 1$ corresponds to DNS. The higher values of M represent the resolution of more of the eddies in the flow field. The sub-grid kinetic energy, k_{SGS} is computed as follows (Pope, 2000):

$$k_{SGS} = \left(\frac{v_{SGS}}{C_k \Delta} \right)^2 \text{ where } C_k = 0.094 \quad (12)$$

4. Results

Fig. 4a shows the oil plume after the plume reached quasi periodic behavior. The plume is opaque within $x/d < 14$, but then one notes large clearances (see for example the dashed lines at $x/d = 14$ at the

top and bottom of the plume, $x/d = 32$ at the bottom part of the plume, $x/d = 42$ throughout the plume and $x/d = 54$ at the bottom part of the plume). These clearances are most likely due to both variability in the oil discharge (experimental errors) and the fact that the velocity ratio was not too large $r = u_{oil}/u_\infty = 5.0$. Ghosh and Hunt (1998) identified the velocity ratio smaller than 10.0 as a strong crossflow. In the experiments of Kohli and Bogard (2005) for film cooling applications, the velocity ratio was 0.38. Morton and Ibbetson (1996) conducted experiments in a wide range of velocity ratio from unity to 100. Davidson and Pun (1999) compared vertical jet (no crossflow) and weakly advected jet in their experiments with velocity ratio of 238.

The predicted oil trajectory was compared to the experimental one in Fig. 4. The upper and lower boundaries of the plume (colored red) obtained from the snapshot in the experiment were superimposed on the instantaneous iso-surface of oil holdup predicted by modified solver (Fig. 4b). Before modifying the solver to add the rise velocity of droplets, large eddy simulation was conducted using standard solver and compared to the plume trajectory observed in the experiment. However, the plume deflected more in crossflow direction with slower rise and the plume trajectory was not captured. For the sake of brevity, the results without adding the rise velocity were not shown here. After adding rise velocity of 5 cm/s, the trajectory of the lower boundary of the plume matched well with the experiment (Fig. 4b). The meandering behavior which is clear along the upper boundary of the plume were also captured in the simulation. However, the upper boundary of the plume rose slower in the simulation. The large droplets which rise faster determine the position of the upper boundary of the plume. The droplet rise velocity was computed based on the d_{50} diameter obtained from the experiments near the lower boundary of the plume. The time series of d_{50} diameter with standard deviation obtained from the top and bottom shadowgraph cameras are shown in Fig. 5. The mean d_{50} diameter was computed to be 1.6 mm near the lower boundary of the plume and 4.4 mm near the upper boundary of the plume.

Larger droplets rise faster than smaller ones due to their higher buoyancy. The terminal rise velocity of a spherical oil droplet with a diameter of 1.6 mm is 5 cm/s, while that of a diameter 4.4 mm is 11 cm/s based on the experiments by Friedman and Katz (2002). In the numerical simulation, the constant rise velocity of 5 cm/s was used in the whole domain, therefore, the upper boundary of the plume was not captured well. In reality, the droplet rise velocity must be assigned to each individual droplet locally after each time step based on their size, and as the simulation did not resolve the droplets, there was no way to assign a value for each cell. Therefore, a constant rise velocity of 5 cm/s was assigned to each droplet in this work. This allowed capturing the lower boundary of the plume as seen in Fig. 4b. However, the upper boundary was underestimated by the numerical solution. In order to estimate the upper boundary of the plume with rise velocity of 11 cm/s,

the vertical position of the plume without rise velocity (estimated by LES simulation) was compared against the vertical position of the plume with rise velocity of 5 cm/s (estimated by LES simulation) and the relative vertical motion of the plume was revealed for the rise velocity of 5 cm/s. Based on the comparison, the plume centerline moves vertically 4.1d at $x/d = 16$ and 10.9d at $x/d = 48$ with rise velocity of 5 cm/s. Applying linear proportion based on this observation, the plume centerline with rise velocity of 11 cm/s was expected to rise 9.0d at $x/d = 16$ and 24.0d at $x/d = 48$ relative to the plume centerline without rise velocity. The location of the upper boundary based on the rise velocity of 11 cm/s was plotted as dashed line in Fig. 4b. The estimated and observed upper boundaries of the plume match well in Fig. 4b.

The current approach is not able to account for the varying rise velocity across droplets of different size present in the physical experiment. In wastewater applications dealing with sludge settling, the settling velocity of sludge flocs can be empirically estimated as a function of local sludge concentration (Takács et al., 1991; Lakehal et al., 1999). However, this may not be an option for the present work which involves buoyant droplets within complex flow field with coherent structures. Moreover, assigning varying rise velocity for different-sized droplets cannot be an ultimate solution for the near field of the jet since the droplet size distribution keep changing due to breakage and coalescence of the droplets. The distribution of different-sized droplets across the whole plume and the boundaries of the plume can be estimated through Eulerian or Lagrangian approaches by considering breakage and coalescence of droplets through population balance model. Recently, Aiyer et al. (2019) adopted Eulerian approach and estimated overall droplet size distribution across an oil plume in crossflow by solving concentration equation for each size bin with breakage term. The present authors, Cui et al. (2020a,b) coupled Lagrangian particle tracking method (Cui et al., 2018) with population balance model called VDROP (Zhao et al., 2014) and computed ultimate DSD for breaking waves by considering both breakage and coalescence effects.

4.1. Oil holdup from the simulation

Instantaneous and time-averaged contours of oil holdup along the central plane are shown in Fig. 6. The contour plot near the orifice was magnified and inserted in (a). The oil jet moves vertically with a slight bending up to $z/d = 3$. Following $z/d = 3$, the vertical oil jet started to bend over in the crossflow direction continuously until $z/d = 12$. The angle between the crossflow and the jet path became almost constant as of $\sim 30^\circ$ beyond $z/d = 12$. In the magnified image, continuous wavy pattern was observed along the upstream surface of the jet up to $z/d = 8$ which was broken down due to axial disturbances. Oil ligaments and oil pockets formed near the orifice downstream due to the surface breakup induced by azimuthal disturbances. The axial and azimuthal disturbances were also reported for liquid jet in gaseous crossflow by Behzad et al. (2016). The oil pockets are tightly-spaced near field of the orifice and separated more in the far field which can be considered as the nature of expanding and diluting oil jet. Many of the oil pockets above $z/d = 20$ were elongated perpendicular to the jet path which is probably due to the shearing effect of crossflow on oil pockets. The time-averaged oil holdup contours in Fig. 6b reveals the dilution rate of oil along the jet path. The oil holdup decreased from unity (at orifice) to 0.1 within only $14d$ vertical distance from the orifice and kept decreasing along the jet path. Around $z/d = 40$, the oil concentration decreased to 1% of the initial concentration. It is also clear that the highest oil holdup was predicted to be closer to the upper boundary of the plume near the orifice. The time-averaged contours of oil holdup at different cross-sections were shown in Fig. 6(c–f). It is clear at P1 and P2 that higher oil concentration was obtained closer to the upper boundary of the plume. The dilution of oil was also clear along the jet path. Kidney-shaped oil distribution was observed at the cross-sections

which was induced by the motion of counter-rotating vortex pair.

The decrease in the oil concentration in vertical direction was compared against prior experimental measurements conducted by Cheung (1991) and the integral model results by Jirka (2004). The normalized centerline dilution, $S_c L_Q L_m / L_b^2$ (see Eq. (2)) of the numerical results is reported as a function of normalized vertical distance, z/L_b in Fig. 7. In the integral model of Jirka (2004), the Gaussian profiles were assumed for the velocity and the concentration yielding the highest velocity and concentration along the jet centerline. However, in this work, the maximum concentration was not observed along the centerline (Fig. 6b). For this reason, we selected the maximum oil concentration at each cross-section in the plume regardless of the location of that maximum, as done in Cheung (1991). For our simulation, the quantities L_Q (Eq. (2a)), L_m (Eq. (2b)) and L_b (Eq. (2c)) were computed to be 0.022 m, 0.111 m and 0.060 m, respectively.

In the integral model of Jirka (2004), the normalized dilution was always smaller than the measurements of Cheung (1991) which indicates that the dilution rate according to the integral model is slower than reality. In this work, before $z/L_b = 1.2$, the dilution is almost unity since the jet did not start to dilute. In the range of $1.2 < z/L_b < 1.9$, the numerical predictions are close to the measurements. In the range of $1.9 < z/L_b < 3.0$, the dilution was predicted close to the integral model results, and at $z/L_b = 2.4$, the estimated dilution rate matched with the integral model. Beyond $z/L_b = 2.4$, the predicted normalized dilution followed the same trend with prior studies. The normalized vertical distance $z/L_b = 2.4$ corresponds to $z = 0.14$ m which is close to the jet-to-plume transition length scale, L_m (0.15 m) (Eq. (2d)), beyond which the buoyancy plays a major role. In contrast to the experiments of Cheung (1991) in which hot water was injected into water, immiscible oil which remains as discrete droplets inside the water was injected herein. The discrete droplets are expected to separate from the entrained water due to their individual buoyancy (Socolofsky et al., 2002). Therefore, the plume rises higher in immiscible jets in crossflow due to the discrete phase separation which was observed by Murphy et al. (2016) by comparing miscible and immiscible jets in crossflow. The transition observed at $z/L_b = 2.4$ in Fig. 7 can be related to this behavior. At the same vertical distance of two plumes with different rising height (penetration to the crossflow), the dilution was expected to be lower for the plume rising faster since the distance taken along the plume path will be shorter, which justifies the lower dilution after $z/L_b = 2.4$ in this work with immiscible fluids.

4.2. Flow field from the simulation

Contours of horizontal (crossflow-wise) and vertical (jet-wise) velocity components are reported in Fig. 8 with velocity details at specific points. In (a) and (b), instantaneous and time-averaged contours of horizontal velocity are shown, respectively. The portion of the pipe and the pipe orifice are pointed out in (a). Upstream of the pipe, the uniform crossflow speed of 0.27 m/s was observed. The horizontal velocity decreased gradually along the upstream side of the jet near the orifice due to crossflow-jet interaction. The crossflow changed its direction towards $-x$ direction just behind the orifice where the wake vortices started to occur. The reverse flow near the orifice with velocity of -0.15 m/s was pointed out in (b). The reverse flow was also observed downstream of the pipe which was induced through the vortex shedding from the solid pipe surface. The highest horizontal velocity of nearly 0.54 m/s was estimated to be at $z/d = 8$ above the orifice locally. The maximum horizontal velocity kept decreasing along the jet path due to the water entrainment and became similar to the crossflow speed after $x/d \approx 80$. The instantaneous and time-averaged contours of vertical velocity are shown in Fig. 8(c,d). The zoom-in image showing the shear layer vortices just above the orifice was inserted in (c). The shear layer vortices were highly unsteady and were not observed in the time-averaged contours. Negative vertical velocity towards the orifice was observed in the regions occupied by the shear layer vortices in the

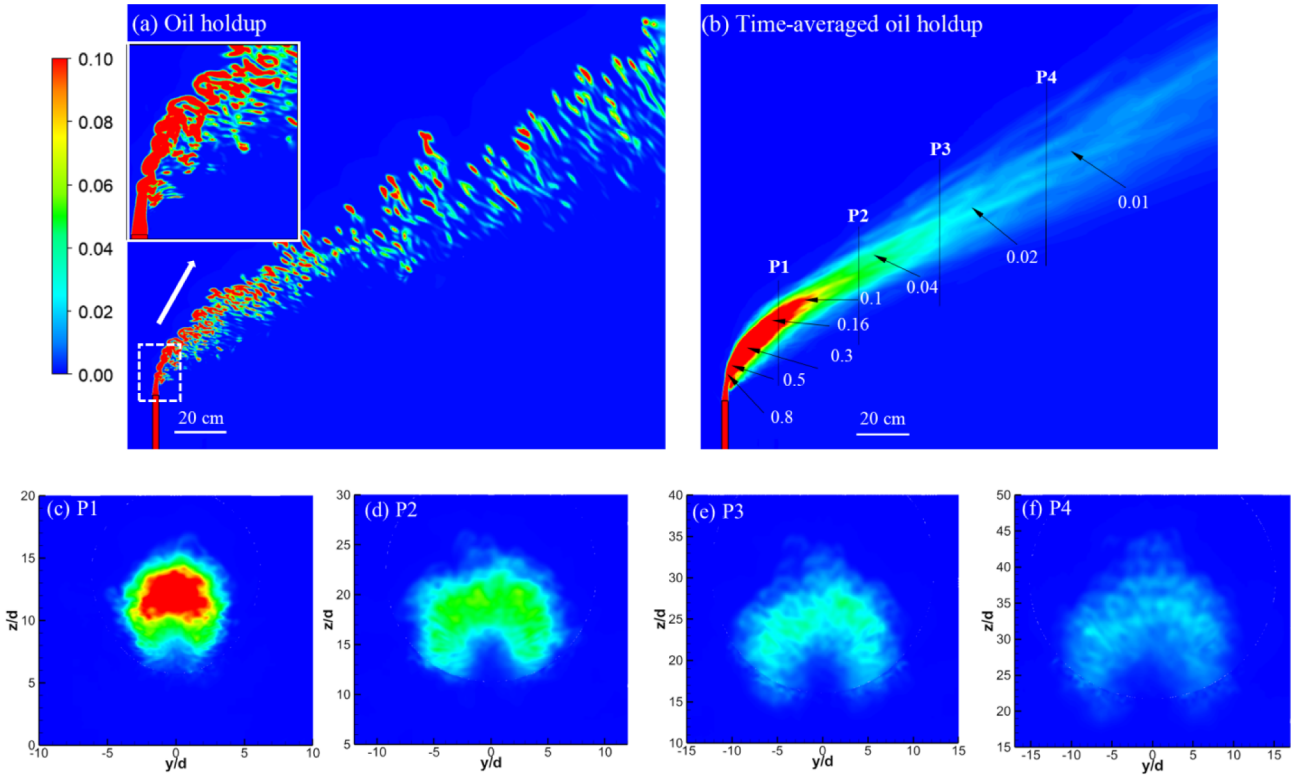


Fig. 6. (a) Instantaneous and (b) time-averaged contours of oil holdup at center plane, and time-averaged oil holdup contours at different cross-sections P1-P4 looking downstream. The instantaneous contours were acquired at $t = 12$ s through large eddy simulation. Note that the axes at cross-section plots have different scales.

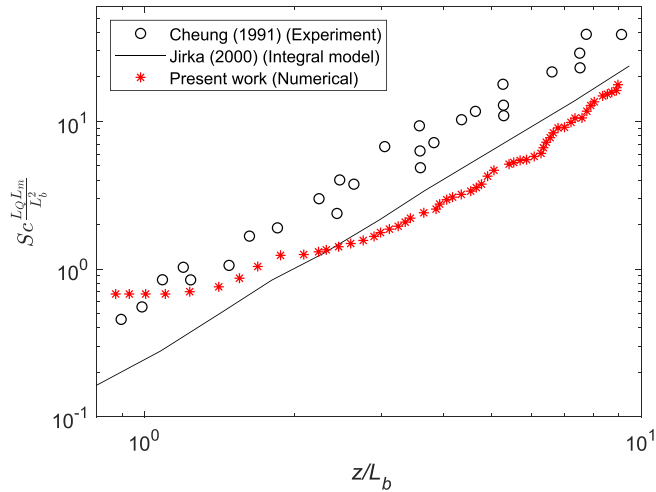


Fig. 7. Normalized centerline dilution $S_c L_Q L_m / L_b^2$ (Eq. (2)) as a function of normalized vertical distance, z/L_b . Here, L_Q is the discharge length scale, L_m is the jet-to-crossflow length scale and L_b is the plume-to-crossflow length scale.

upstream and downstream side of the jet with a magnitude of 0.1 m/s. At the orifice, sheared velocity profile was observed due to pipe entrance, and a maximum velocity of ~2.0 m/s was observed along the centerline. At $z/d = 8$, the maximum vertical velocity decreased to 0.5 m/s. The sudden decrease in vertical velocity from 1.9 m/s to 0.5 m/s was observed in the range of $4 < z/d < 8$. At $x/d = 16$ and $z/d = 16$ which is beyond the jet-to-plume transition length scale, the vertical velocity decreased suddenly and kept its level around 0.1 m/s to 0.2 m/s after that region. Therefore, we consider the vertical flow was mainly dominated by the buoyancy forces and the secondary flows induced by counter-rotating vortex pair for the region beyond that

transition zone. Prior to the transition zone (jet dominated zone), it is clear in (b) and (d) that the highest horizontal and vertical velocity were obtained closer to the upper boundary of the plume which contradicts the assumption of the highest velocity along the jet centerline in the integral model (Jirka, 2004) for the jet-in-crossflow.

Time-averaged contours of spanwise velocity in y direction and velocity vectors are shown at different cross-sections in Fig. 9. At each cross-section, positive spanwise velocity was observed in the top-right and bottom-left while the negative spanwise velocity was observed in the top-left and bottom-right. The magnitude of the spanwise velocity was around 0.05 m/s which is < 20% of the crossflow velocity. The spanwise velocity kept decreasing as the jet moved further downstream. By noting velocity vectors, it is fair to conclude that the spanwise velocity was induced through the CVP (discussed later). The spanwise velocity contours reveal four subzones with high-velocity as two rows and two columns (2×2). The spanwise velocity between these sub-zones was almost zero at all cross-sections. At P1 (near field of the jet), the regions occupied with positive and negative velocities ordered smoothly and resemble ellipsoid shapes. The high-velocity regions expand $12d$ in spanwise direction and $15d$ in jet-wise direction. At P2 and further, the positive-negative velocity regions in the second row kept their smoothly-curved shapes while the ones in the upper row were disturbed due to crossflow-plume interaction. The high-velocity regions expanded more in spanwise and jet-wise directions as the jet moves further downstream. At P4, the high-velocity regions expand $26d$ in both spanwise and jet-wise directions.

The numerical predictions were compared against ADV data. The location of each ADV is listed in Table 2. ADV1 is outside of the plume and its elevation is close to the upper boundary of the plume estimated in the numerical simulation. Since the upper boundary of the plume was not captured well in the simulation by employing the constant rise velocity of 5 cm/s, the comparison to the data acquired by ADV1 cannot be made. ADV3 is also near the upper boundary of the plume, however

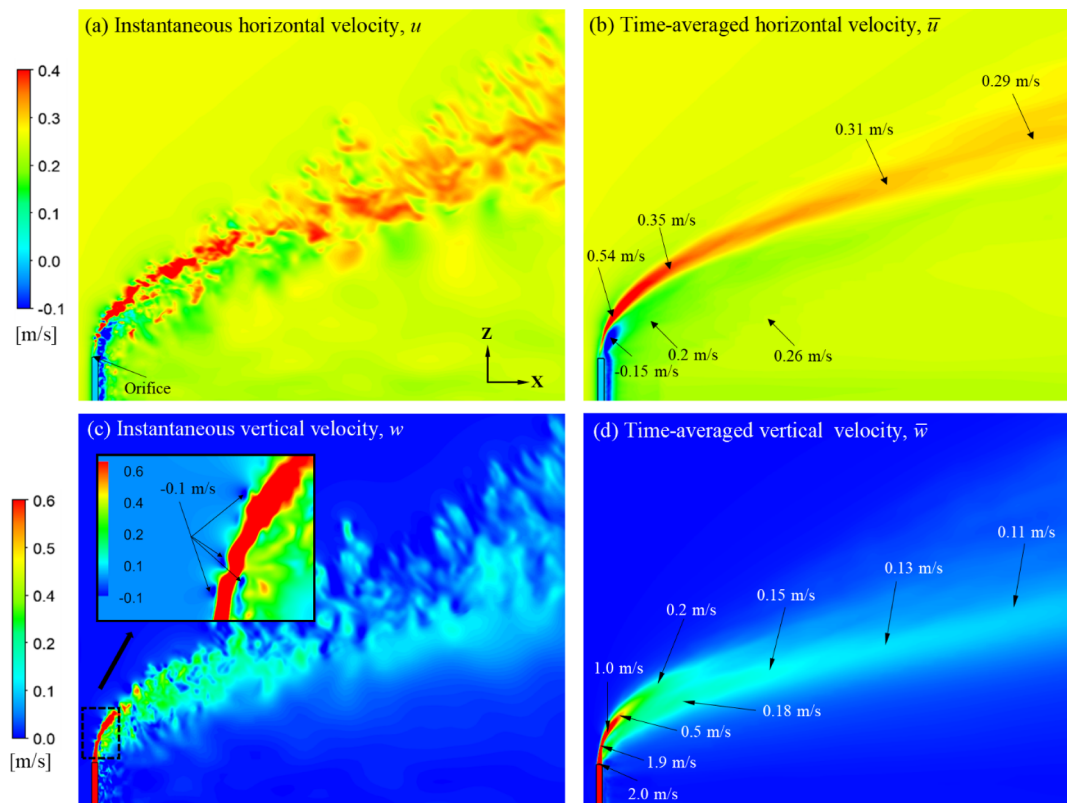


Fig. 8. Instantaneous and time-averaged contours of (a,b) horizontal velocity and (c,d) vertical velocity at the central x - z plane. The instant contours were acquired at $t = 12$ s and time averaging were carried out between the simulation time of 10 s and 19.5 s through large eddy simulation. The left column shows the instantaneous contours while the right column shows the time-averaged contours.

not exactly outside of the plume (at the edge of the plume). Although an agreement was not expected for ADV3, it is presented to elaborate the experimental results. All the velocity data provided by ADV4 had signal-to-noise ratio lower than 15.0, therefore only the velocity components acquired by ADV2 and ADV3 are shown in Fig. 10 along with the numerical predictions. ADV2 is on the left-hand side of the plume while looking downstream and near the lower boundary of the plume while the ADV3 was on right-hand side of the plume and closer to the upper boundary of the plume. To make the images clearer and to avoid the darkness, only one out of eight data points were presented for ADV3. The horizontal streamwise velocity “ u ” was in the range from 0.1 to 0.2 m/s at ADV2, and from 0.1 to 0.3 m/s at ADV3 which covers the towing speed of 0.27 m/s. The simulation provided velocity values of 0.27 m/s at both locations since constant velocity was applied in the crossflow direction, however the pipe was towed in the experiment which resulted in velocity reduction outside of the plume. The spanwise velocity alternated between -0.1 m/s and -0.3 m/s at ADV2 and between -0.1 and 0.1 m/s at ADV3. The negative spanwise velocity acquired by ADV2 most probably indicates the negative velocity induced by CVP vortex (discussed later) along the top-left side of the plume (Fig. 9). The change in the velocity direction at ADV3 can be related to the meandering behavior of the plume. The spanwise velocity at both ADVs was predicted to be around zero in the simulation. The vertical velocity was estimated and measured to be around zero at ADV2. At ADV3, the vertical velocity was measured to be around 0.1 m/s which is close to the rise velocity of the upper boundary of the plume (11 cm/s) based on the droplet size acquired from the upper shadowgraph camera (Figs. 1, 4 and 5).

The time-averaged contour lines of oil holdup and horizontal velocity are superimposed on the flooding contours of vertical velocity at the central x - z plane and shown in Fig. 11. The transverse jet trajectory can be defined based on the local maximum of (i) velocity, (ii)

vorticity, (iii) scalar or (iv) the stream line trajectory initiated from the center of jet exit (Mahesh, 2013). The local maximums of vorticity were obtained near the center of CVP which grows in spanwise direction and deviates from the center plane. Therefore, the jet trajectory of vorticity was not presented herein for consistency. The contour lines of oil holdup at 0.001 and horizontal velocity at 0.27 m/s in the far-field were assumed to present the boundaries of the plume based on the oil holdup and horizontal velocity, respectively. The jet trajectory based on oil holdup penetrates deeper into the crossflow as compared to the trajectory based on horizontal velocity. The primary reason of this difference is the separation of oil droplets from the plume due to their additional rise velocity in vertical direction. The contours of vertical velocity were shown at the center plane and the cross-section. The vertical shifting between the contours of horizontal and vertical velocity might be related to the formation of counter-rotating vortex pair which induced upward velocity near the lower boundary of plume shown in Fig. 11b with velocity vectors. Outside of the centerline where the CVP occurs, the vertical velocity decreased suddenly. The jet trajectory based on local maximum of oil holdup, horizontal velocity and vertical velocity are shown in Fig. 11c. All were showing almost linear behavior in the far-field, therefore linear fit of the data was presented to remove the noisy. Besides, the central streamline originated from the origin of the jet exit was also plotted for comparison purposes. All the jet trajectories except for the jet trajectory based on vertical velocity followed the same path up to $x/d = 15$. After $x/d = 15$ and $z/d = 15$, the vertical distance between the oil holdup trajectory and the center streamline increased along the jet path. At $x/d = 70$, the difference between the trajectories became $14d$. The trajectories of the center streamline, and the horizontal velocity was almost similar up to $x/d = 30$ where the center streamline started to deviate by bending more in crossflow direction. The distance between the trajectories increased gradually and became almost $4d$ at $x/d = 70$. The lower penetration of

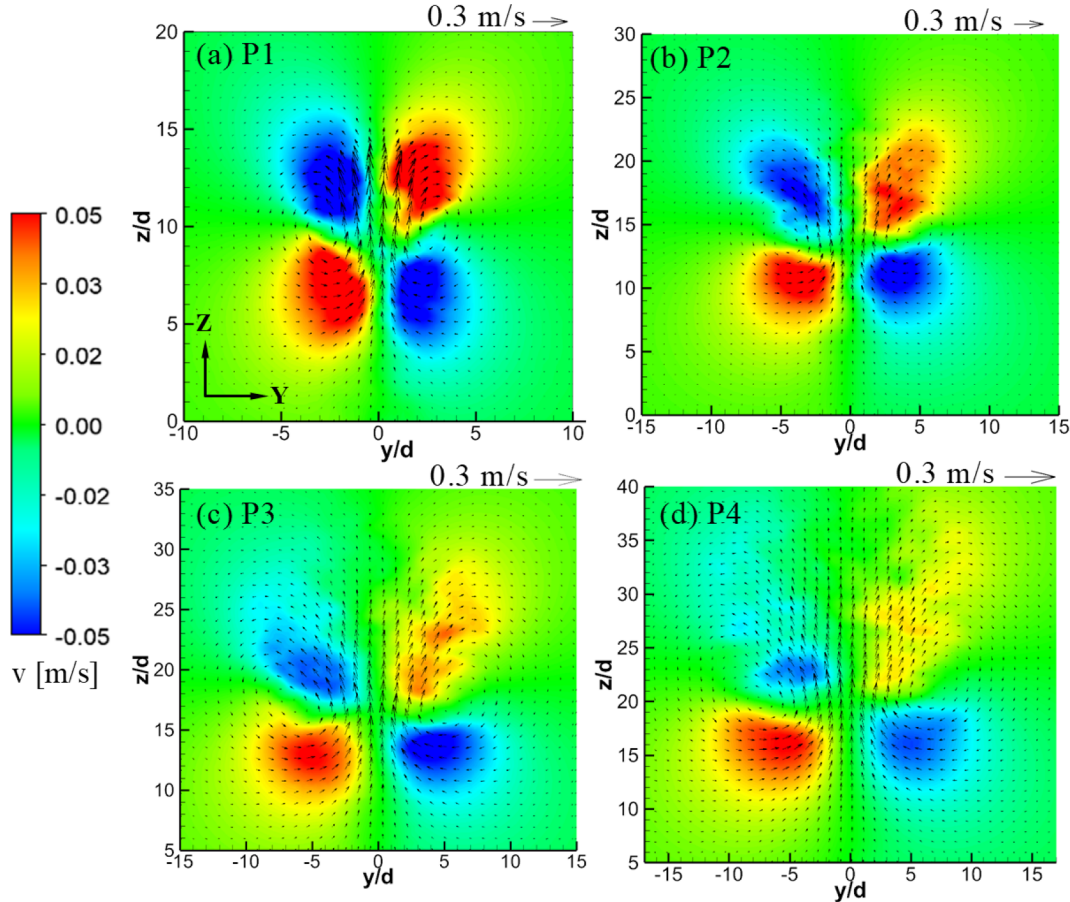


Fig. 9. Time-averaged contours of spanwise velocity and velocity vectors along the cross-sections P1–P4 looking downstream (Fig. 6). The results are acquired through large eddy simulation. Note that the axes have different scales.

the center streamline into the crossflow can be related to the occurrence of the highest vertical velocity along the lower boundary of the plume. Following $x/d = 30$, the trajectories based on vertical velocity and the center streamline were almost parallel with a deviation of $8d$ at $x/d = 70$. The maximum rise of the jet trajectory was observed within the order of oil holdup, horizontal velocity, center streamline and vertical velocity as $47d$, $36d$, $33d$ and $25d$ at the horizontal distance of $70d$.

4.3. Vortical structures from the simulation

Jet flows injected into a crossflow from a wall is characterized with four different types of vortical structures (Fric and Roshko 1994): (i) jet shear layer vortices, (ii) horseshoe vortices, (iii) wake vortices and (iv) counter-rotating vortex pair (CVP). Fig. 12 shows the vortical structures using the Q-criterion (Hunt and Wray, 1988). The horseshoe vortices are usually induced through the interaction between the wall boundary layer at the bottom and the jet flow (Kelso and Smits, 1995). As the pipe orifice was placed 0.7 m above the bottom-wall boundary (Fig. 2), this likely prevented the formation of the horseshoe vortices near the orifice. The shear layer vortices induced by Kelvin Helmholtz (K-H) instabilities started to occur at $z/d = 2$ and were observed clearly along the perimeter of the jet near field. The z -vorticity contours were presented along the x - y plane at $z/d = 2$ to show the rotation direction of the wake vortices. As shown in Fig. 12, the alternating vortices near the jet wake was induced by elongated vortical structures beneath the plume. One side of the wake vortices were connected to the leeward side of the plume. The wake vortices numbered in Fig. 12 reveals that the positive and the negative vortices created a regular sequential pattern. The wake vortices (1), (3) and (5) rotates in $-z$ direction while the wake vortices (2) and (4) rotates in $+z$ direction. The strength of

the vorticity along the plane decreased far-wake of the jet due to the plume rise and the blending of the jet with the crossflow.

The counter-rotating vortex pair are shown in Fig. 13 along the y - z plane at different distances from the orifice: (a) P1, $x/d = 8$, (b) P2, $x/d = 20$, (c) P3, $x/d = 32$ and (d) P4, $x/d = 48$. The velocity vectors were also superimposed on the vorticity contours to reveal the vertical motion induced by CVP along the centerline. As compared to other vortices, the CVP persisted further downstream as observed by Mahesh (2013) too. At P1, the CVP were obtained along $-5 < y/d < 5$ in spanwise direction and $4 < z/d < 16$ in jet-wise direction. Higher vorticity was obtained in larger space in jet-wise direction. The mean jet centerline passes through the $y/d = 0$ as expected due to the axisymmetric flow domain. The flow moves in clockwise direction on the right side of the jet centerline while moving counter-clockwise direction on the left side of the jet centerline. Along the lateral sides of the plume, the flow moves downward in $-z$ direction. The highest vertical velocity was observed along the centerline in upward $+z$ direction. The vorticity outside of the plume was predicted to be almost zero due to lack of velocity gradients. At P2, the plume expanded in both directions and was obtained along $-8 < y/d < 8$ in spanwise direction and $8 < z/d < 24$ in jet-wise direction. The localized CVP at P1 started to dissipate in both directions. The lateral distance between the vortices was increased as compared to the CVP at P1. The positive vortex on the right-hand side at P2 tilted in clockwise direction while the negative vortex on the left-hand side tilted in counter-clockwise direction. Small-sized vortices were observed above the vortex pair rotating in both positive and negative directions. At P3 and P4, the vortex pair were obtained closer to the leeward side of the plume. The strength of the CVP decreased in crossflow-wise direction due to the jet expansion induced by water entrainment and blending of the plume with the

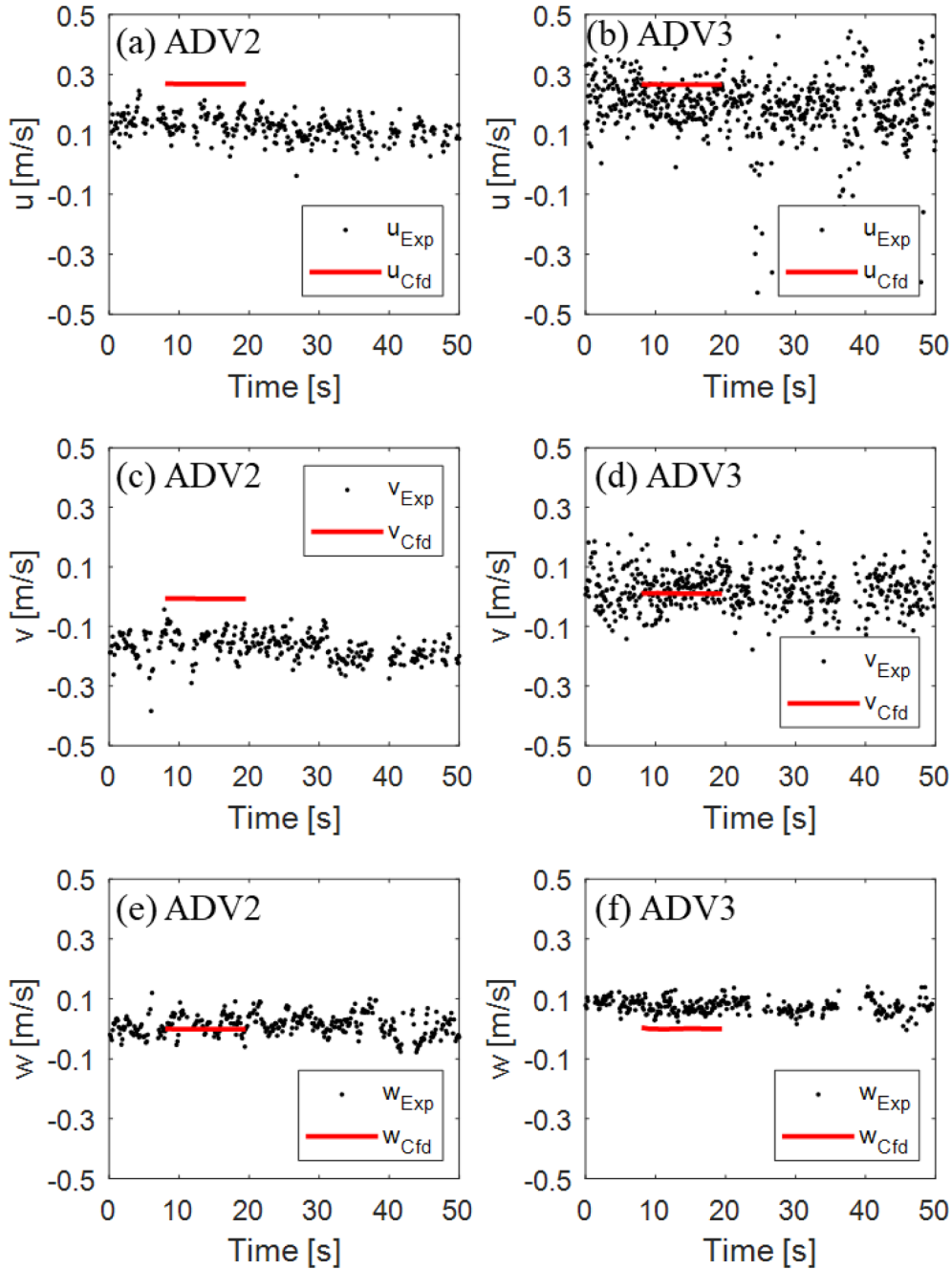


Fig. 10. Time series of velocity components acquired by ADV2 (left column) and ADV3 (right column): (a,b) u velocity (crossflow direction), (c,d) v velocity (spanwise direction) and (e,f) w velocity (jet-wise direction).

crossflow with lower turbulence.

4.4. Turbulent kinetic energy (t.k.e.) from the simulation

The resolved t.k.e. was computed based on Eq. (9). Time-averaged contours of the normalized turbulent kinetic energy with the mean center streamline are shown on the center plane in Fig. 14a. The resolved turbulent kinetic energy was normalized based on upstream velocity and velocity ratio as $\frac{k_{res}}{u_{\infty}^2 r^2}$. Yuan et al. (1999), and Muppudi and Mahesh (2007) presented similar contours of resolved t.k.e. which were obtained through LES and DNS, respectively. The maximum normalized t.k.e. was reported to be around 0.1 and 0.135 by Yuan et al. (1999) ($r = 3.3$), and Muppudi and Mahesh (2007) ($r = 5.7$), respectively. In this work in which the velocity ratio is 5.0, the maximum normalized

t.k.e. was predicted to be almost 0.1 just above the jet exit. The interaction between the crossflow and the oil jet induced higher t.k.e. along the leading and trailing edges of the jet which collided later near the center streamline at $s/d = 3$ where s is the direction along the jet path.

The variation of the resolved t.k.e. along the center streamline was plotted in Fig. 14b. At the center of the jet exit, the t.k.e. was almost zero until the collapsing of high-t.k.e. zones at the leading and trailing edges of the jet. The zero t.k.e. at the jet exit ($s/d = 0$) is directly related to the almost zero t.k.e. along the pipe centerline. In contrast to our observations, the normalized t.k.e. at the jet exit was predicted to be < 0.01 in Muppudi and Mahesh (2007) which is 6% of the maximum t.k.e. observed in their direct numerical simulation. Almost zero t.k.e. along the pipe centerline in our work can be related to the no-perturbation condition at pipe entrance. The mean t.k.e. reached its maximum

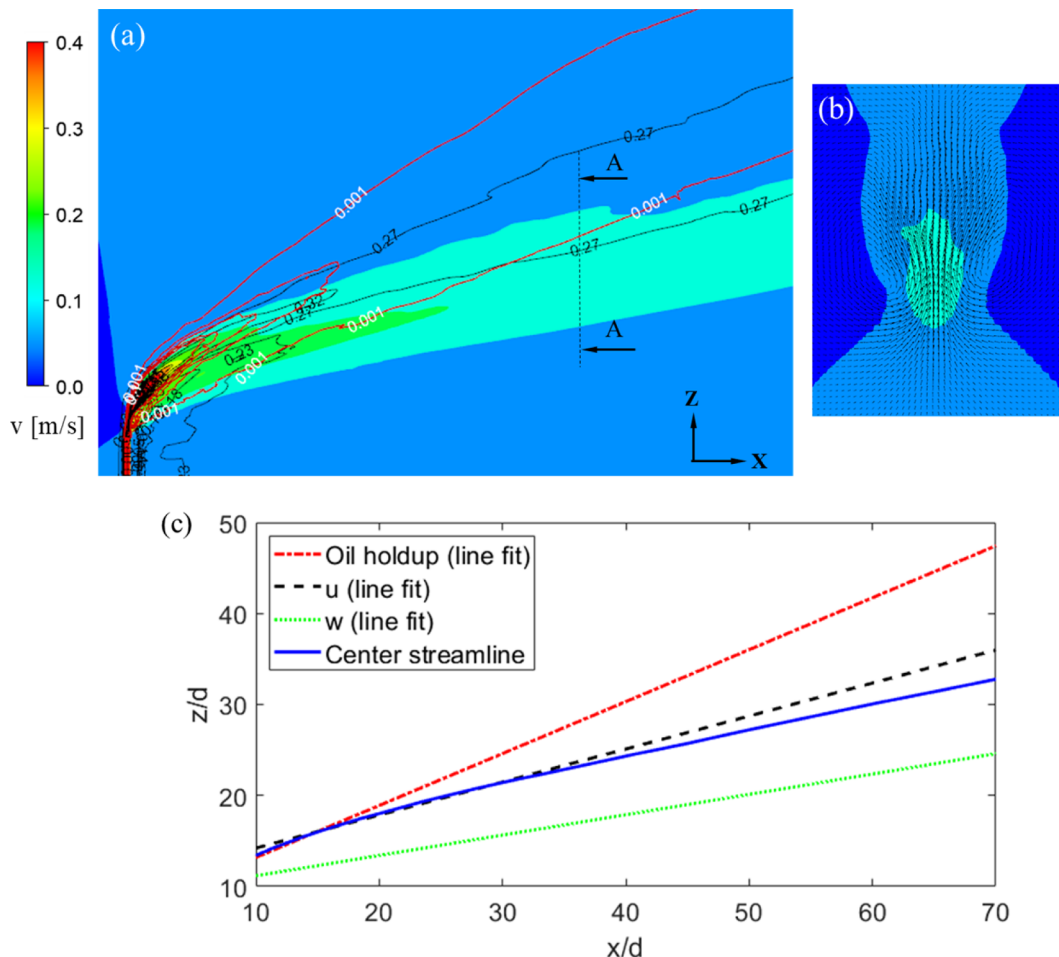


Fig. 11. (a) Time-averaged contour lines of oil holdup (colored red) and horizontal velocity (colored black) which are superimposed on the contours of vertical velocity at the central x - z plane, and (b) the contours of vertical velocity and velocity vectors at y - z plane at $x/d = 70$ (cross-section A-A in (a)). (c) The jet trajectory based on oil holdup, horizontal velocity, vertical velocity and center streamline. The results are acquired through large eddy simulation. (For interpretation of the references to colour in this figure legend, the reader is referred to the web version of this article.)

at $s/d = 5$ and decreased gradually to 6% of its maximum at $s/d = 25$. The location of the maximum t.k.e. and the characteristics of the t.k.e. variation curve presented herein mainly concur with DNS results of Muppudi and Mahesh (2007) (Fig. 12 in their paper).

To judge the quality of LES, the ratio of resolved t.k.e. to total t.k.e. was computed based on Eq. (11) and shown in Fig. 15 along vertical lines at different horizontal distances from the pipe orifice. The other component of total t.k.e., the sub-grid (residual) t.k.e., was computed based on Eq. (12). The resolved part of the t.k.e. was found to exceed 80% of the total t.k.e. in the most portion of the plume cross-section at the central plane. The ratio became around 0.75 in a small region near the lower boundary of the plume where the CVP vortices were observed (Fig. 13). Based on the criteria established by Pope, (2000), as the contribution of resolved part (energy containing motions) is 80%, the accuracy of LES can be justified.

5. Conclusions

Large eddy simulation coupled with mixture multiphase model was performed for an oil jet in crossflow. Experimental results obtained by towing the pipe horizontally in Ohmsett wave tank were presented. The oil jet velocity was 1.36 m/s in vertical direction while the crossflow (towing) velocity was 0.27 m/s in horizontal direction which yielded velocity ratio of 5.0. The pictures of the droplets were taken using shadowgraph camera near the upper and lower boundaries of the plume at a horizontal distance of 2 m from the orifice (Figs. 1 and 4). Using

standard multiphase model undershot the whole plume trajectory. The solver was modified to include the transport term due to the rise velocity of oil droplets. Using d_{50} (volume-median) droplet size near the lower boundary of the plume (Fig. 5) enabled us to capture lower boundary of the plume however, the estimated upper boundary of the plume penetrated less into the crossflow (Fig. 4). Comparing the plume trajectory obtained by the standard and the modified solvers allowed us to estimate the plume elevation based on the rise velocity. The upper boundary of the plume was estimated using the rise velocity of the d_{50} obtained by upper shadowgraph camera with a good agreement (Fig. 4). The droplets were too small to resolve therefore, we could not use a systematic approach to allow the upper boundary of the plume to spread more to mimic the observations.

The oil holdup was estimated to be unity up to $z = 3d$ and decreased suddenly to 0.1 at $z = 14d$ (Fig. 6). Near field of the jet, oil holdup was higher close to the upper boundary of the plume. Kidney-shaped oil holdup was observed at the cross-section of the plume due to the CVP vortices. The predicted oil dilution rate along the jet trajectory was compared to integral model by Jirka (2004) (Fig. 7). The horizontal velocity was doubled locally near the upper boundary of the plume at $z = 8d$ and reverse flow was observed along the trailing edge near the orifice (Fig. 8 (a-b)). The shear layer vortices created negative vertical (downward) velocity along the leading and trailing edges of the jet up to $z = 8d$ (Fig. 8(c,d)). The jet trajectory based on oil holdup penetrated more into the crossflow as compared to the center streamline trajectory due to the separation of discrete oil phase from entrained water due to

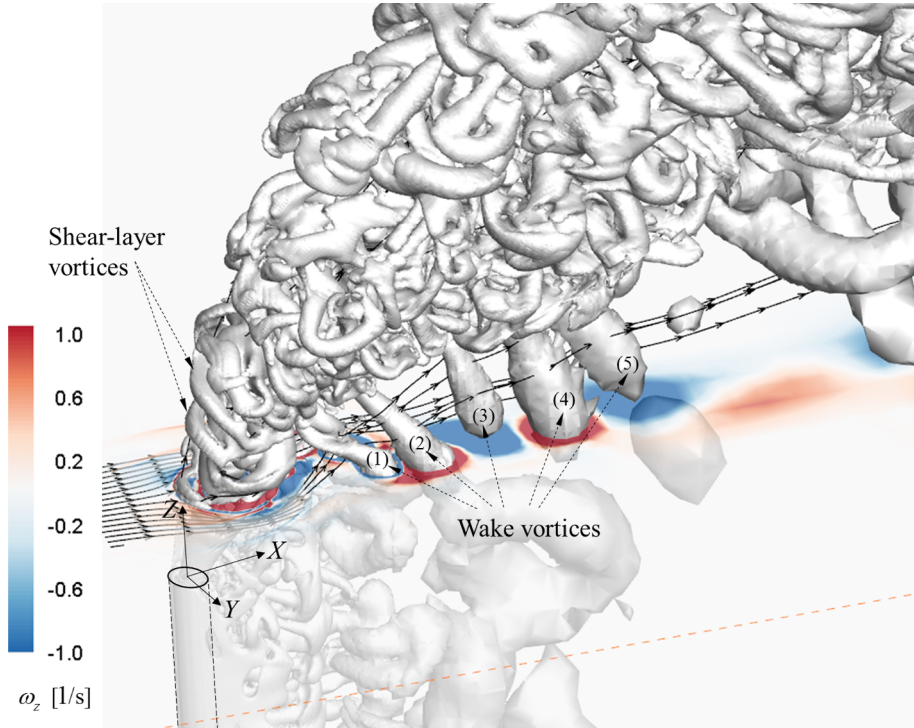


Fig. 12. Instantaneous iso-surface of Q-criterion at a value of $1.0 \text{ } 1/\text{s}^2$ at $t = 10.3 \text{ s}$ showing two types of vortical structures: shear-layer vortices and wake vortices (tornado-like). The contours of z -vorticity (rotation in horizontal plane) are provided in the horizontal plane ($x-y$ plane) at $z/d = 2.0$. The streamlines initiated on the $x-y$ plane upstream of the jet was presented to reveal the flow motion before and after the jet. The results are acquired through large eddy simulation.

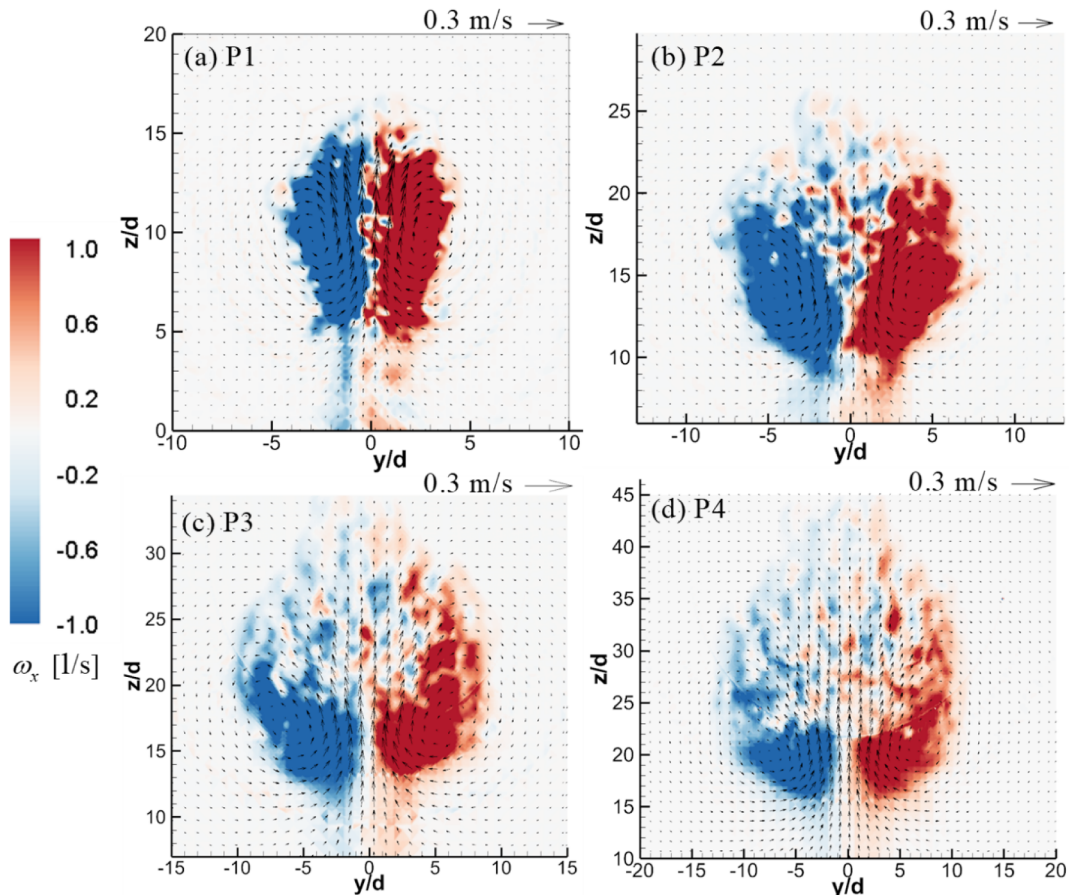


Fig. 13. Contours of x -vorticity (rotation in vertical crossflow plane) computed using time-averaged velocity at cross-sections P1-P4 looking downstream (Fig. 6). The time-averaged velocity vectors are also shown. The kidney-shaped counter-rotating vortex pair (CVP) was observed clearly at each cross-section presented herein. The results are acquired through large eddy simulation. Note that the axes have different scales.

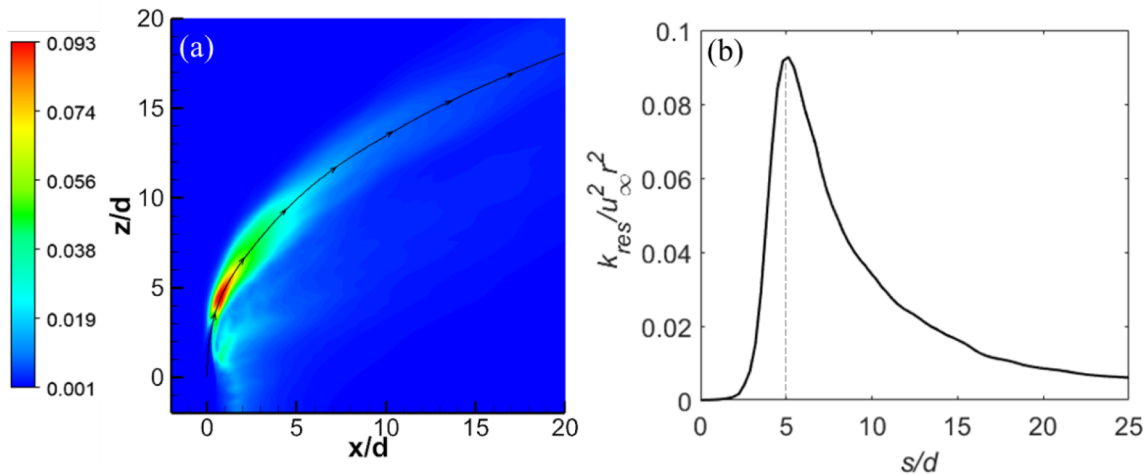


Fig. 14. (a) Normalized resolved turbulent kinetic energy at center plane and the mean center streamline, (b) the variation of normalized turbulent kinetic energy along the center streamline up to $s/d = 25$.

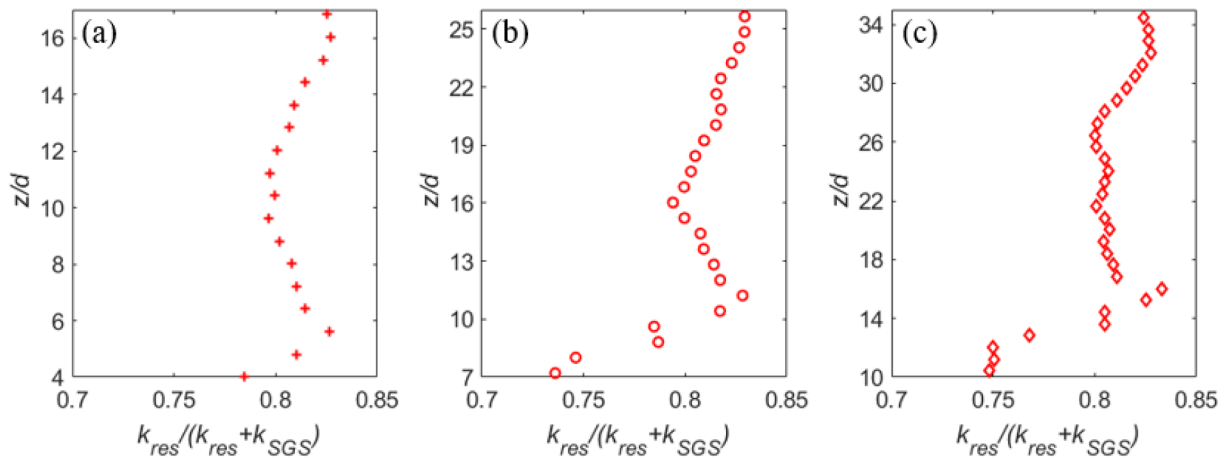


Fig. 15. The ratio of resolved turbulent kinetic energy to total turbulent kinetic energy along the vertical lines (at center plane) at (a) $x/d = 8$, (b) $x/d = 20$ and (c) $x/d = 32$. The initial position of each vertical line was decided based on the lower boundary of the vertical velocity contour in Fig. 11a while the end of each vertical line was decided based on the upper boundary of oil holdup contour in Fig. 11a to cover the whole region including oil or high-velocity gradient.

their buoyancy (Socolofsky et al., 2002) (Fig. 11).

The CVP covered almost the whole cross-section of the plume and played a major role in the jet hydrodynamics (Fig. 13). Small-sized eddies were observed above the CVP vortices created due to the interaction between the jet and the crossflow. The CVP created upward velocity along the plume centerline near the lower boundary of the plume (Fig. 8d and 11b) and relatively smaller downward velocity near the lateral sides of the plume (Fig. 9). Elongated wake vortices were created from the leeward side of the plume and showed an alternating vorticity pattern without expanding in spanwise direction as much as the CVP (Fig. 13). The formation of CVP is expected to promote the mixing of chemicals and droplets within the plume.

CRediT authorship contribution statement

Cosan Daskiran: Methodology, Investigation, Writing - original draft. **Fangda Cui:** Methodology, Software. **Michel C. Boufadel:** Conceptualization, Project administration, Writing - review & editing, Funding acquisition. **Lin Zhao:** Validation, Investigation. **Scott A. Socolofsky:** Methodology, Validation, Formal analysis. **Tamay Ozgokmen:** Resources, Project administration, Funding acquisition. **Brian Robinson:** Resources, Conceptualization. **Thomas King:** Resources, Conceptualization.

Declaration of Competing Interest

The authors declare that they have no known competing financial interests or personal relationships that could have appeared to influence the work reported in this paper.

Acknowledgments

The authors gratefully acknowledge support by the Department of Fisheries and Oceans (DFO) Canada through Multi-Partner Research Initiative grant: MECTS-39390783-v1-OFSCP. Funding from the Centre for Offshore Oil, Gas and Energy Research, COOGER is also acknowledged. This work used the Extreme Science and Engineering Discovery Environment (XSEDE), which is supported by National Science Foundation grant number TG-BCS190002. Specifically, we used the Comet system, which is an NSF-funded system operated by the San Diego Supercomputer Center at UC San Diego.

References

- Aiyer, A., Yang, D., Chamecki, M., Meneveau, C., 2019. A population balance model for large eddy simulation of polydisperse droplet evolution. *J. Fluid Mech.* 878, 700–739.
- Behzad, M., Ashgriz, N., Karney, B., 2016. Surface breakup of a non-turbulent liquid jet injected into a high pressure gaseous crossflow. *Int. J. Multiph. Flow* 80, 100–117.
- Bodart, J., Coletti, F., Bermejo-Moreno, I., Eaton, J., 2013. High-fidelity simulation of a

- turbulent inclined jet in a crossflow. *CTR Annu. Res. Briefs* 19, 263–275.
- Brackbill, J.U., Kothe, D.B., Zemach, C., 1992. A continuum method for modeling surface tension. *J. Comput. Phys.* 100 (2), 335–354.
- Cheung, V. (1991). “Mixing of a round buoyant jet in a current.” Ph.D. Thesis, University of Hong Kong, Hong Kong.
- Coletti, F., Benson, M., Ling, J., Elkins, C., Eaton, J., 2013. Turbulent transport in an inclined jet in crossflow. *Int. J. Heat Fluid Flow* 43, 149–160.
- Cui, F., Boufadel, M.C., Geng, X., Gao, F., Zhao, L., King, T., Lee, K., 2018. Oil droplets transport under a deep-water plunging breaker: Impact of droplet inertia. *J. Geophys. Res. Oceans* 123 (12), 9082–9100.
- Cui, F., Daskiran, C., King, T., Robinson, B., Lee, K., Katz, J., Boufadel, M.C., 2020a. “Modeling oil dispersion under breaking waves. Part I: Wave hydrodynamics.”. *Environ. Fluid Mech.*
- Cui, F., Zhao, L., Daskiran, C., King, T., Lee, K., Katz, J., Boufadel, M.C., 2020b. “Modeling oil dispersion under breaking waves. Part II: Coupling lagrangian particle tracking with population balance model.”. *Environ. Fluid Mech.*
- Davidson, M., Pun, K., 1999. Weakly advected jets in cross-flow. *J. Hydraul. Eng.* 125 (1), 47–58.
- Erlebacher, G., Hussaini, M.Y., Speziale, C.G., Zang, T.A., 1992. Toward the large-eddy simulation of compressible turbulent flows. *J. Fluid Mech.* 238, 155–185.
- Fabregat, A., Dewar, W.K., Özgökmen, T.M., Poje, A.C., Wienders, N., 2015. Numerical simulations of turbulent thermal, bubble and hybrid plumes. *Ocean Model.* 90, 16–28.
- Fabregat, A., Poje, A.C., Özgökmen, T.M., Dewar, W.K., 2016. Dynamics of multiphase turbulent plumes with hybrid buoyancy sources in stratified environments. *Phys. Fluids* 28 (9), 095109.
- Fischer, H., E. List, R. Koh and J. Imberger (1979). Mixing in Inland and Coastal Waters. New York.
- Francois, M., Sicilian, J., Kothe, D.B., 2007. “Modeling interfacial surface tension in fluid flow.”. Oak Ridge National Laboratory, Oak Ridge, TN.
- Fric, T., Roshko, A., 1994. Vortical structure in the wake of a transverse jet. *J. Fluid Mech.* 279, 1–47.
- Friedman, P., Katz, J., 2002. Mean rise rate of droplets in isotropic turbulence. *Phys. Fluids* 14 (9), 3059–3073.
- Galeazzo, F.C.C., Donnert, G., Cárdenas, C., Sedlmaier, J., Haberleiter, P., Zarzalis, N., Beck, C., Krebs, W., 2013. Computational modeling of turbulent mixing in a jet in crossflow. *Int. J. Heat Fluid Flow* 41, 55–65.
- Ghosh, S., Hunt, J., 1998. Spray jets in a cross-flow. *J. Fluid Mech.* 365, 109–136.
- Gopalan, S., Abraham, B.M., Katz, J., 2004. The structure of a jet in cross flow at low velocity ratios. *Phys. Fluids* 16 (6), 2067–2087.
- Hamam, S.E., 1987. Diffusion of crude oil in water. *J. Environ. Sci. Health Part A* 22 (5), 445–456.
- Hunt, G., Van den Bremer, T., 2011. Classical plume theory: 1937–2010 and beyond. *IMA J. Appl. Math.* 76 (3), 424–448.
- Hunt, J. C., A. A. Wray and P. Moin (1988). “Eddies, streams, and convergence zones in turbulent flows.”.
- Jirka, G.H., 2004. Integral model for turbulent buoyant jets in unbounded stratified flows. Part I: Single round jet. *Environ. Fluid Mech.* 4 (1), 1–56.
- Jirka, G.H., Domeker, R.L., 1991. Hydrodynamic classification of submerged single-port discharges. *J. Hydraul. Eng.* 117 (9), 1095–1112.
- Joye, S.B., MacDonald, I.R., Leifer, I., Asper, V., 2011. Magnitude and oxidation potential of hydrocarbon gases released from the BP oil well blowout. *Nat. Geosci.* 4 (3), 160.
- Kelso, R., Smits, A., 1995. Horseshoe vortex systems resulting from the interaction between a laminar boundary layer and a transverse jet. *Phys. Fluids* 7 (1), 153–158.
- Kohli, A., Bogard, D.G., 2005. Turbulent transport in film cooling flows. *J. Heat Transfer* 127 (5), 513–520.
- Lakehal, D., Krebs, P., Krijgsman, J., Rodi, W., 1999. Computing shear flow and sludge blanket in secondary clarifiers. *J. Hydraul. Eng.* 125 (3), 253–262.
- Leifer, I., Solomon, E., Schneider, J., Deimling, V., Coffin, R., Rehder, G., Linke, P., 2015. The fate of bubbles in a large, intense bubble plume for stratified and unstratified water: Numerical simulations of 22/4b expedition field data. *J. Marine Petrol. Geol.* 68B, 806–823.
- Lima Neto, I.E., Zhu, D.Z., Rajaratnam, N., 2008. Bubbly jets in stagnant water. *Int. J. Multiph. Flow* 34, 1130–1141.
- Ling, J., Ruiz, A., Lacaze, G., Oefelein, J., 2017. Uncertainty analysis and data-driven model advances for a jet-in-crossflow. *J. Turbomach.* 139 (2), 021008.
- Ma, T., Quintiere, J., 2003. Numerical simulation of axi-symmetric fire plumes: accuracy and limitations. *Fire Saf. J.* 38 (5), 467–492.
- MacDonald, I., Leifer, I., Sassen, R., Stine, P., Mitchell, R., Guinasso, N., 2002. Transfer of hydrocarbons from natural seeps to the water column and atmosphere. *Geofluids* 2 (2), 95–107.
- Mahesh, K., 2013. The interaction of jets with crossflow. *Annu. Rev. Fluid Mech.* 45, 379–407.
- Manninen, M., V. Taivassalo and S. Kallio (1996). On the mixture model for multiphase flow, Technical Research Centre of Finland Finland.
- McGrattan, K.B., Baum, H.R., Rehm, R.G., 1998. Large eddy simulations of smoke movement. *Fire Saf. J.* 30 (2), 161–178.
- McLellan, S.J., Nicholas, A.P., 2000. A new method for evaluating errors in high-frequency ADV measurements. *Hydro. Process.* 14 (2), 351–366.
- McNutt, M., R. Camilli, G. Guthrie, P. Hsieh, V. Labson, B. Lehr, D. Maclay, A. Ratzel and M. Sogge (2011). Assessment of flow rate estimates for the Deepwater Horizon/Macondo well oil spill, Flow Rate Technical Group report to the National Incident Command, Interagency Solutions Group, March 10, 2011.
- Milanovic, I., Zaman, K.B., Bencic, T.J., 2012. Unsteady wake vortices in jets in cross-flow. *J. Visualization* 15 (1), 45–55.
- Morton, B., Taylor, G.I., Turner, J.S., 1956. Turbulent gravitational convection from maintained and instantaneous sources. *Proc. R. Soc. Lond. A* 234 (1196), 1–23.
- Morton, B.R., Ibbetson, A., 1996. Jets deflected in a crossflow. *Exp. Therm Fluid Sci.* 12 (2), 112–133.
- Muldoon, F., Acharya, S., 2006. Analysis of k and epsilon budgets for film cooling using direct numerical simulation. *AIAA J.* 44 (12), 3010–3021.
- Muppudi, S., Mahesh, K., 2007. Direct numerical simulation of round turbulent jets in crossflow. *J. Fluid Mech.* 574, 59–84.
- Murphy, D.W., Xue, X., Sampath, K., Katz, J., 2016. Crude oil jets in crossflow: Effects of dispersant concentration on plume behavior. *J. Geophys. Res. Oceans* 121 (6), 4264–4281.
- Nortek, A., 1998. ADV operation manual. Vollen, Norway, pp. 34.
- Pope, S., 2000. Turbulent Flows. Cambridge University Press.
- Pope, S.B., 2004. Ten questions concerning the large-eddy simulation of turbulent flows. *New J. Phys.* 6 (1), 35.
- Qu, X., Khezzar, L., Danciu, D., Labois, M., Lakehal, D., 2011. Characterization of plunging liquid jets: A combined experimental and numerical investigation. *Int. J. Multiph. Flow* 37 (7), 722–731.
- Ruiz, A., Lacaze, G., Oefelein, J., 2015. Flow topologies and turbulence scales in a jet-in-cross-flow. *Phys. Fluids* 27 (4), 045101.
- Rusche, H., 2003. Computational fluid dynamics of dispersed two-phase flows at high phase fractions. Imperial College London (University of London).
- Ryan, K.J., Bodart, J., Folkersma, M., Elkins, C.J., Eaton, J.K., 2017. Turbulent scalar mixing in a skewed jet in crossflow: experiments and modeling. *Flow Turbulence Combust.* 98 (3), 781–801.
- Sallam, K., Faeth, G., 2003. Surface properties during primary breakup of turbulent liquid jets in still air. *AIAA J.* 41 (8), 1514–1524.
- Shinjo, J., Matsuyama, S., Mizobuchi, Y., Ogawa, S., Umemura, A., 2009. A numerical study on ligament disintegration mechanism by propagative capillary waves. *Atomization* 18, 36–43.
- Shinjo, J., Umemura, A., 2011. Detailed simulation of primary atomization mechanisms in diesel jet sprays (isolated identification of liquid jet tip effects). *Proc. Combust. Inst.* 33 (2), 2089–2097.
- Smagorinsky, J., 1963. General circulation experiments with the primitive equations: I. The basic experiment. *Mon. Weather Rev.* 91 (3), 99–164.
- Socolofsky, S., Adams, E., 2002. Multi-phase plumes in uniform and stratified crossflow. *J. Hydraul. Res.* 40 (6), 661–672.
- Socolofsky, S.A., Adams, E.E., Sherwood, C.R., 2011. Formation dynamics of subsurface hydrocarbon intrusions following the Deepwater Horizon blowout. *Geophys. Res. Lett.* 38 (L09602), 1–6.
- Socolofsky, S.A., Crouse, B.C., Adams, E.E., 2002. Multiphase plumes in uniform, stratified, and flowing environments. *Environ. Fluid Mech. Theories Appl.* 85–125.
- Som, S., Aggarwal, S., 2010. Effects of primary breakup modeling on spray and combustion characteristics of compression ignition engines. *Combust. Flame* 157 (6), 1179–1193.
- Takács, I., Patry, G.G., Nolasco, D., 1991. A dynamic model of the clarification-thickening process. *Water Res.* 25 (10), 1263–1271.
- Tian, X., Roberts, P.J., 2003. A 3D LIF system for turbulent buoyant jet flows. *Exp. Fluids* 35 (6), 636–647.
- Wegner, B., Huai, Y., Sadiki, A., 2004. Comparative study of turbulent mixing in jet in cross-flow configurations using LES. *Int. J. Heat Fluid Flow* 25 (5), 767–775.
- Wright, S.J., 1977. Mean behavior of buoyant jets in a crossflow. *J. Hydraulics Division* 103, 12944.
- Yang, D., Chen, B., Socolofsky, S.A., Chamecki, M., Meneveau, C., 2016. Large-eddy simulation and parameterization of buoyant plume dynamics in stratified flow. *J. Fluid Mech.* 794, 798–833.
- Yousefi-Lafouraki, B., Ramiar, A., Ranjbar, A.A., 2016. Numerical simulation of two phase turbulent flow of nanofluids in confined slot impinging jet. *Flow Turbulence Combust.* 97 (2), 571–589.
- Yuan, L.L., Street, R.L., Ferziger, J.H., 1999. Large-eddy simulations of a round jet in crossflow. *J. Fluid Mech.* 379, 71–104.
- Zhao, L., Torlapati, J., Boufadel, M.C., King, T., Robinson, B., Lee, K., 2014. VDROP: A comprehensive model for droplet formation of oils and gases in liquids-Incorporation of the interfacial tension and droplet viscosity. *Chem. Eng. J.* 253, 93–106.